Spatio-temporal foreshock evolution of the 2019 M 6.4 and M 7.1 Ridgecrest, California earthquakes

Hui Huang [a], Lingsen Meng [a,*], Roland Bürgmann [b], Wei Wang [c], Kang Wang [b]

[a] *Earth Planetary and Space Sciences, University of California, Los Angeles, CA 90025, USA*
[b] *Berkeley Seismological Laboratory and Department of Earth and Planetary Science, University of California, Berkeley, CA 94720, USA*
[c] *Department of Earth Sciences, University of Southern California, Los Angeles, CA 90089, USA*

ARTICLE INFO

ABSTRACT

The 2019 M 6.4 and M 7.1 Ridgecrest, California earthquake sequence provides an ideal opportunity to study the seismicity evolution and interaction among multiple complex fault structures. Here, we apply the matched-filter detection method to obtain a relatively complete (magnitude of completeness ≈ 0.9) and precisely relocated earthquake catalog. The results show a short-duration (∼ 31 minutes) foreshock sequence with 28 events, before the M 6.4 earthquake. The foreshock sequence started with a M 4.0 event and was aligned along the NW-SE direction. This implies that the M 6.4 rupture initiated on a NW trending fault segment, before rupturing the primary SW trending fault. Repeating earthquakes before and after the M 7.1 event are separated in space and bound the areas of large coseismic slip in the M 6.4 and M 7.1 events. This might reflect local slow slip acceleration near the edges of coseismic rupture asperities. The NW-striking fault zones illuminated by seismicity are separated into several sub-regions with distinct pre-M7.1 seismicity rate evolutions. The M 7.1 event nucleated in a region of local seismicity concentration which intensified ∼ 3 hr before the M 7.1 mainshock. The M 7.1 nucleation zone is characterized by a significantly low b value of events that occurred since the M 6.4 event, which might indicate local failure conditions approaching a critical state.

© 2020 Elsevier B.V. All rights reserved.

1. Introduction

On 5 July 2019, the Mw 7.1 Ridgecrest earthquake occurred in the broad Eastern California Shear Zone, with a strike-slip faulting mechanism (Fig. 1a). The M 7.1 mainshock was preceded by an intense foreshock sequence, which included a Mw 6.4 event that occurred ∼ 34 hours earlier. The M 6.4 event was followed by abundant aftershocks, both along SW- and NW-striking faults (Fig. 1a). The M 6.4 event ruptured both SW- and NW- trending fault planes, with the primary slip along the SW-trending fault (Figs. 1b and 1c). In contrast, aftershocks of the M 7.1 event were mainly distributed along a primarily NW striking fault zone, and along at least 20 orthogonal faults cutting across the main fault (Ross et al., 2019). The multiple fault segments involved in the M 6.4 and M 7.1 events provide a rare opportunity to investigate how earthquake sequences evolve in complex fault systems, which is important to improve our understanding of fault interactions, earthquake triggering, and evolving earthquake hazard during an ongoing earthquake sequence.

Small earthquakes are important to illuminate the fault structure as well as the evolution of an earthquake sequence. In addition, small events are also key to understanding the preparation and nucleation process of large earthquakes (e.g., Bouchon et al., 2011, Kato et al., 2012). However, due to the low signal-to-noise ratio and/or overlapping waveforms, the routine earthquake catalogs usually miss a significant portion of small events. The matched-filter detection method is based on exploiting the waveform similarity of events occurring at similar locations (Gibbons and Ringdal, 2006). It has been widely used to detect low-frequency earthquakes (e.g., Shelly et al., 2007) as well as to obtain more complete records of foreshock or aftershock sequences down to low magnitudes (e.g., Peng and Zhao, 2009, Kato et al., 2012, Huang et al., 2017).

Foreshock sequences are inferred to be manifestations of mainshock nucleation processes and have been observed to precede a number of recent large earthquakes (e.g., Bouchon et al., 2013, Ellsworth and Bulut, 2018, Kato et al., 2012, Socquet et al., 2017). The foreshock sequences may be driven by static stress transfer between consecutive events (cascade model) or background aseismic slip (preslip model). Various physical mechanisms can contribute to advancing the evolution towards rupture nucleation along fault systems. Static stress changes induced by previous earthquake

* Corresponding author.
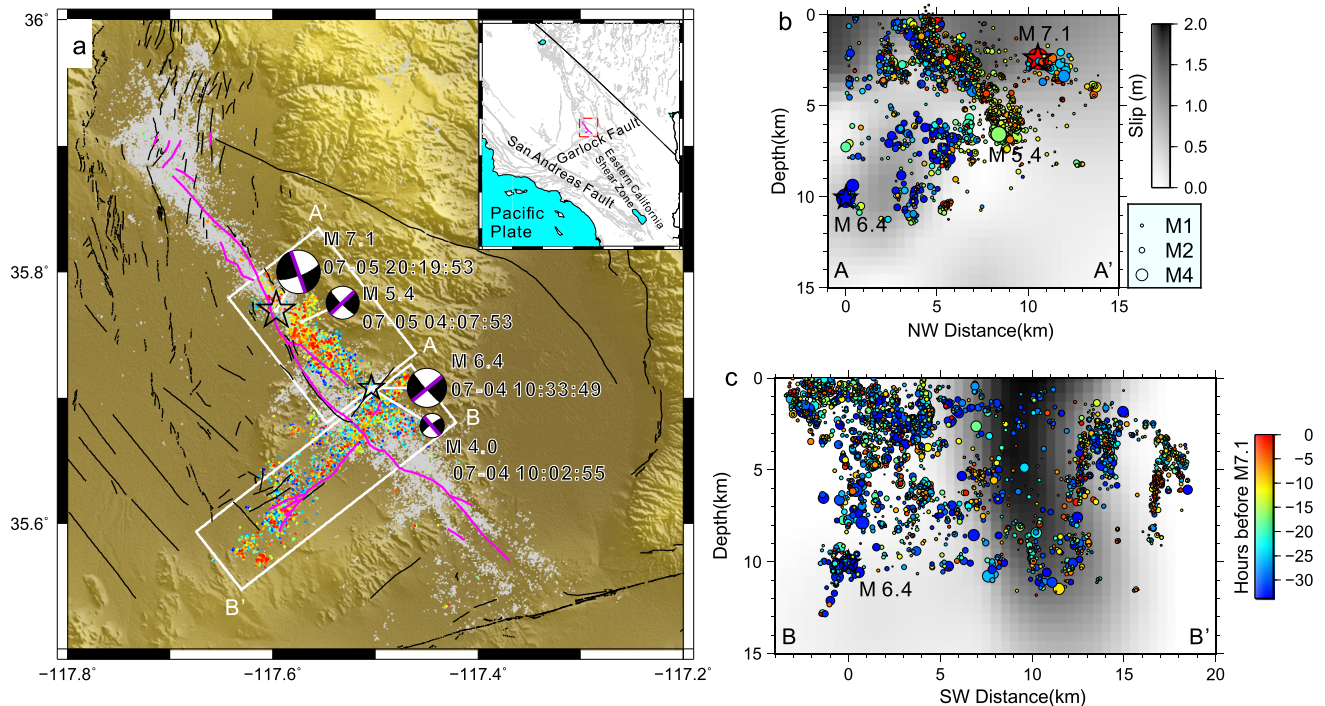*E-mail address:* meng@ess.ucla.edu (L. Meng).

Fig. 1. (a) Relocated seismicity (gray dots) from 1 January to 1 August 2019. The black lines are Quaternary fault traces and the magenta lines denote the surface rupture traces (Milliner and Donnellan, 2020). The focal mechanisms were obtained from USGS, with the purple thick lines highlighting the fault planes. The M 6.4 and M 7.1 fault planes are inferred from the coseismic slip model (Wang et al., 2020) while the M 4.0 and M 5.4 fault planes are inferred from their aftershocks. Their origin times (local time) are labeled. The events after M 6.4 and before M 7.1 are colored by time. (b) and (c) show the depth profiles of seismicity along profile AA' and BB' (origin at the M 6.4 epicenter), respectively. The background is shaded with the M 6.4 coseismic slip model from Wang et al. (2020), derived from a combination of strong motion, GPS and InSAR datasets. (For interpretation of the colors in the figure(s), the reader is referred to the web version of this article.)

ruptures can permanently change the Coulomb stress in nearby regions and promote the occurrence of earthquakes at locations of positive stress change. On the other hand, dynamic stresses can induce temporary stress perturbations during the passage of body and/or surface waves (Hill and Prejean, 2015). In addition, other physical processes such as aseismic slip or fluid diffusion can also progressively alter the stress field and/or frictional properties of the fault to trigger seismicity (e.g., Shelly et al., 2016). It is an ongoing debate whether distinctive features exist and allow foreshocks recognizable as precursory phenomena prior to eventual mainshocks (e.g., Shearer, 2012; Ogata and Katsura, 2014; Seif et al., 2018).

From an earthquake catalog built from matched-filter detections, Ross et al. (2019) document a prominent foreshock sequence before the M 6.4 event. In addition, they suggest that seismic activity on the part of the NW-striking fault separating the M 6.4 rupture intersection from the M 7.1 hypocenter, eroded away barriers to slip during the 34 hour delay between the M 6.4 and M 7.1 events. In this study, we utilize the matched-filter method to detect and relocate events (including mainshock hypocenters) in a similar time period but focus on the detailed evolution of small events relative to the hypocenters of the M 6.4 and M 7.1 events. We identify repeating earthquakes from the waveform analysis, which are possible indicators of aseismic slip. In addition, we explore the b-value variations from the magnitude-frequency statistics, which may indicate variations in faulting style, fault zone complexity or stress conditions along the fault zone (e.g., Petruccelli et al., 2019 and references therein). Our results shed new light on the nucleation processes of the M 6.4 and M 7.1 events.

2. Data and methods

We collect continuous seismograms from 1 January to 1 August 2019, recorded by 35 local broadband and short-period stations

(Figure S1). We select 25,227 template events from 1 January to 8 September 2019 listed in the Southern California Earthquake Data Center (SCEDC) catalog, with the requirement that both horizontal and vertical uncertainties are smaller than 1 km. The data processing steps generally follow previous studies (e.g., Peng and Zhao, 2009, Huang and Meng, 2018). Template waveforms are extracted from 3-component seismograms at each station, starting from 2 sec before and ending 6 sec after the theoretical S-wave arrival times. The travel times are estimated based on a 1D velocity model in southern California (Hutton et al., 2010). Both template and continuous waveforms are filtered by a two-way, fourth-order Butterworth filter with a frequency band of 2 - 8 Hz. To reduce the computational cost, the data are downsampled to 20 Hz. We also require at least 12 high-quality channels (signal-to-noise ratio >= 5, see equation in Figure S2) for each template event. The template waveforms are slid through the continuous data with a step size of 0.05 sec (1 data point) and the cross-correlation coefficient (CC) is calculated at each time step. Then the CC traces for all channels are stacked after accounting for the different travel times at each station. We define positive detections as those with CC exceeding 12 times the median absolute deviation of the CC traces on the day of interest (Figure S2), comparable with previous studies (e.g., Huang and Meng, 2018). If multiple detections are associated with the same segment of the continuous data (within 4 sec), only the one with the highest CC is kept. The location of the detected event is initially assigned at the location of the associated template. The magnitude of the detected event is estimated based on the median of the peak amplitude ratios between the template and detected waveforms, using a scaling coefficient estimated at each station (Figure S3). One example of detecting a foreshock of the M 6.4 event is shown in Figure S2.

We implement the relocation of the template and detected events together using the Growclust algorithm (Trugman and Shearer, 2017a). We form event pairs by linking each event with
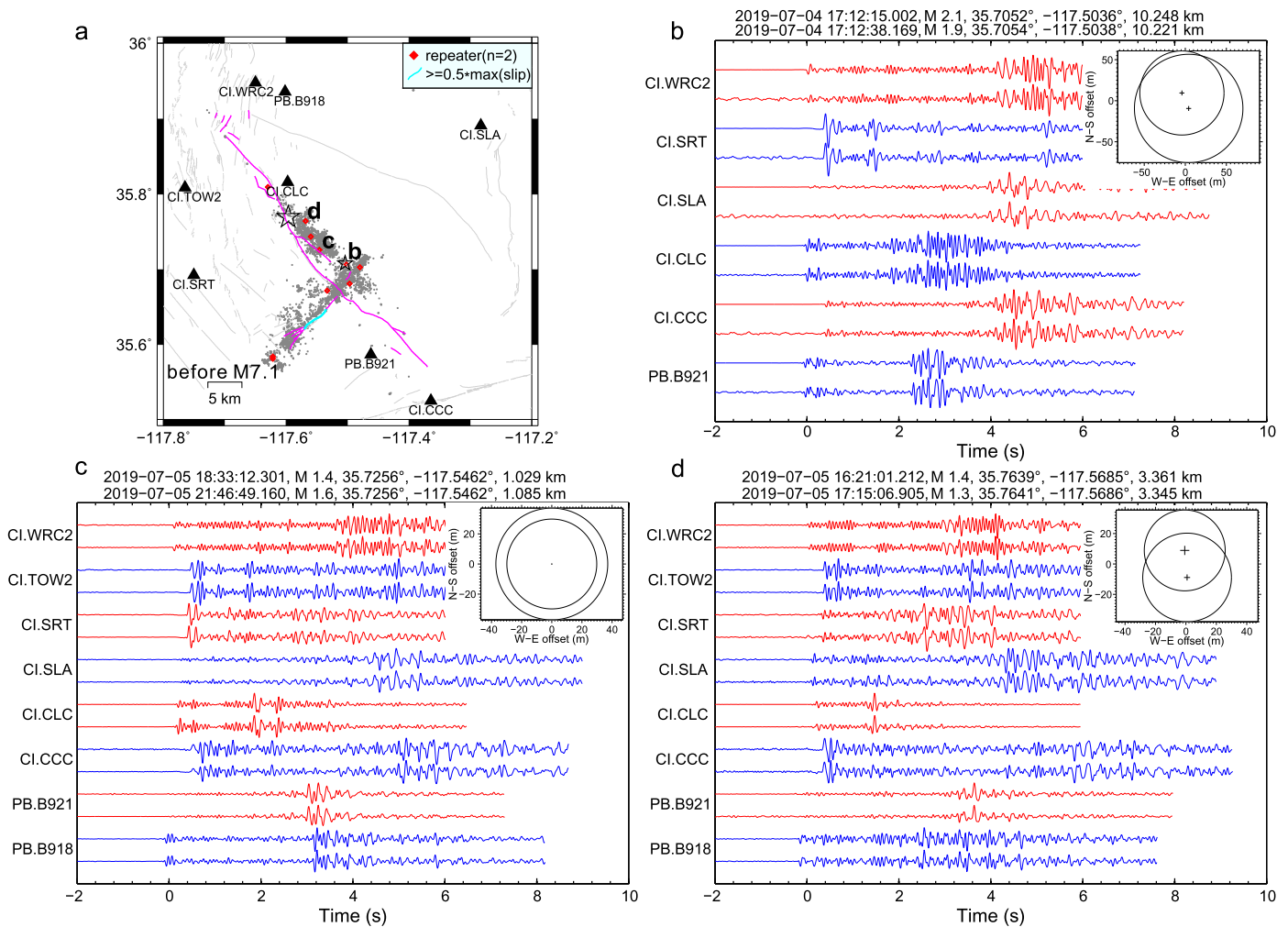
Fig. 2. (a) shows the seismicity (gray dots) and repeaters (red diamonds) during the period from January 2019 to the M 7.1 event. Note that there are only doublet-type repeaters (n = 2) in this time period. The cyan lines highlight the portion of the surface rupture traces along which more than half of the maximum M 6.4 coseismic slip occurred (Wang et al., 2020). (b)-(d) show vertical waveforms (filtered at 2-16 Hz) for example repeating earthquake doublets, with locations shown in (a). The inset panels show the overlapping source patches (assuming 3 MPa stress drop) with the horizontal relative location errors plotted as bars at the respective epicenters. The earthquake information is shown above the panel with origin times in UTC.

all nearby template events that fall within 5 km. The differential travel times are measured by cross-correlating P and S waveforms (filtered at 2-16 Hz, with 100 Hz sampling rate) centered at theoretical arrival times or at manually picked arrival times when available in the SCEDC catalog. We keep the differential times only if the CCs are larger than 0.7 and the delay times measured on both 1 and 1.5 sec cross-correlation windows are consistent (<= 0.01 sec). This step is useful to mitigate the chance of spuriously high correlations due to correlating noise or cycle skipping (Waldhauser and Schaff, 2008). The sub-sample precision of the delay time is achieved by fitting a parabolic curve around the peak CC (Figure S4). Note that the waveform similarity generally breaks down for event pairs with large magnitude differences, thus it is challenging to relocate major events relative to other smaller events. In order to relocate the hypocenters of the M 6.4 and M 7.1 events, we cross correlate their initial onset (0.15 and 0.3 sec) waveforms (raw data) with nearby small events to estimate travel time differences (Figure S4). This procedure was previously used to relocate hypocenters of other mainshocks (e.g., Ellsworth and Bulut, 2018; Yoon et al., 2019).

We identify repeating earthquakes based on waveform similarity and source overlap (e.g., Lengliné and Marsan, 2009, Meng et al., 2015). To detect more potential recurrences of repeaters, we include later catalog events (from 1 August 2019 to 1 May 2020)

into analysis. We first identify candidate repeater pairs with significant waveform similarity. We calculate the maximum CC between all waveform pairs for events with hypocentral separations smaller than 5 km. The vertical components are filtered between 2 and 16 Hz and windowed from 2 sec before P arrival times to 5 sec after S arrivals, similar to the time window used in previous studies (e.g., Uchida and Matsuzawa, 2013; Meng et al., 2015). We define the candidate repeater pairs with CC $\geq$ 0.9 at 6 or more stations. Then, we further require the magnitude difference to be smaller than 0.5 and at least 50% overlap of source areas (along the horizontal direction) between the relocated candidate repeater pairs (e.g. Figs. 2b-2d). In addition, we require that the horizontal location error for each candidate event is smaller than 0.3 times the source radius. The source radius of each event is estimated based on the relationship of seismic moment and stress drop. The moment of each earthquake is converted from the magnitude and the stress drop is assumed to be 3 MPa for all earthquakes (Equations S4-S5, Text S1). Under these criteria, however, it is still possible that some of the identified repeater pairs represent two close sources due to the uncertainties in relative locations and the assumed stress drop. In addition, for M < 2 events, distinguishing repeaters requires higher frequency contents (> 16 Hz) which may be insufficiently resolved in the observed waveforms (Uchida and Bürgmann, 2019).
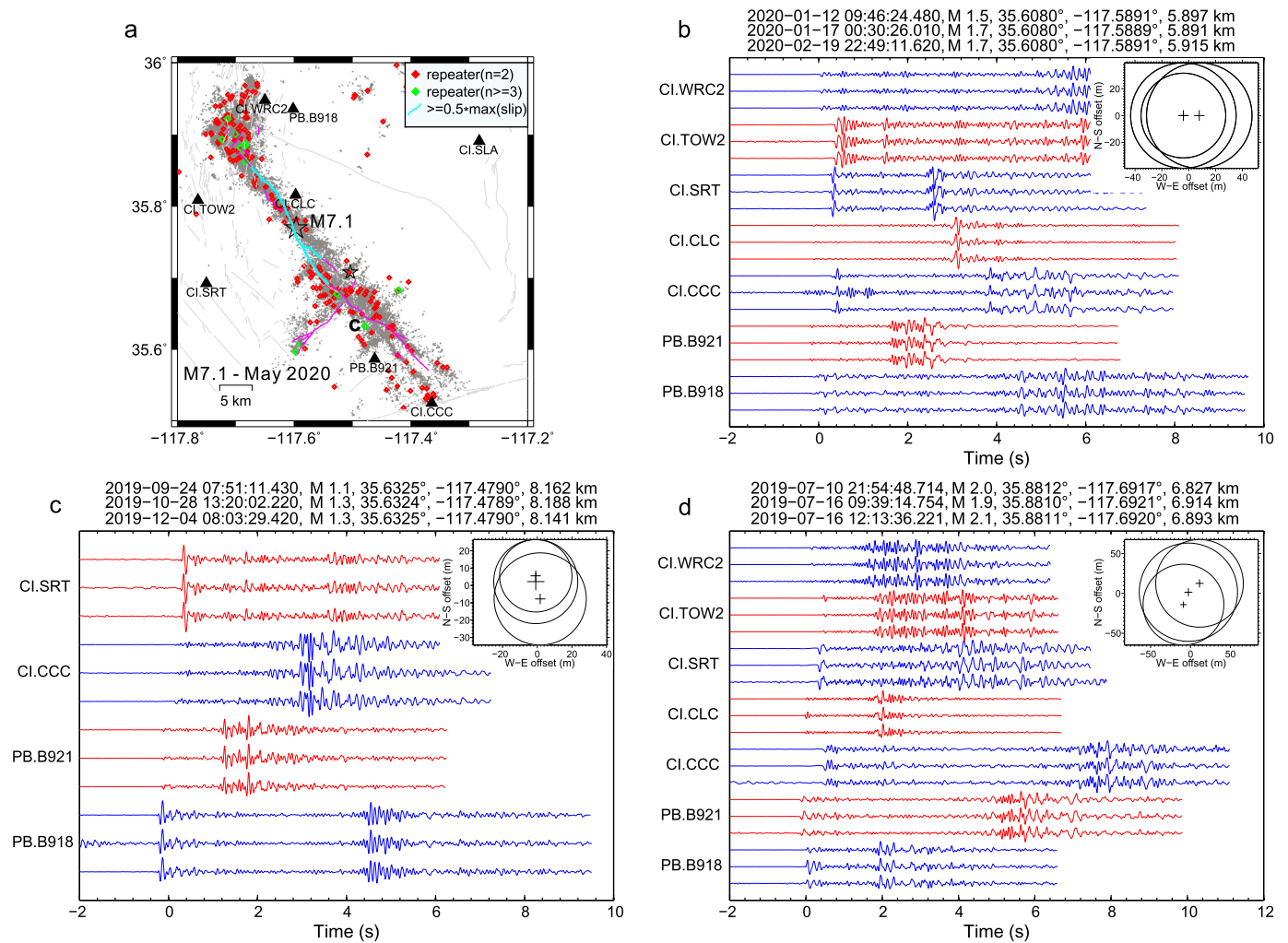
Fig. 3. Similar to Fig. 2 but for the seismicity (gray dots) and repeaters (red and green diamonds) during the period from the M 7.1 mainshock to 1 May 2020. The cyan lines highlight the portion of the surface rupture traces along which more than half of the maximum M 7.1 coseismic slip occurred (Wang et al., 2020). Green diamonds in (a) denote triplet/multiplet (n >= 3) repeating sequences, with example similar waveforms in 3b-3d.

Repeater pairs are merged into the same sequence if they share the same event.

Finally, we estimate the b value for the seismicity occurring in different time periods. The magnitude of completeness (Mc) is first estimated by the Best Combination Method, which combines the goodness-of-fit and maximum curvature methods. The goodness-of-fit method optimizes the fitting to the synthetic frequency-magnitude distribution while the maximum curvature method seeks the point of maximum curvature in the observation (Wiemer, 2001). Then the b value is estimated by the maximum likelihood method based on the events (>= 50) with magnitudes larger than Mc but smaller than 4.0.

3. Results

We detect a total of 84,873 new events (Table S1) from 1 January to 1 August 2019, $\sim$ 4.9 times the number of events listed in the SCEDC catalog. In the new catalog which combines the SCEDC catalog with the newly detected events, 67,834 events ($\sim$ 66%) are relocated. In addition, both the M 6.4 and M 7.1 events are successfully relocated, because of the sufficiently high similarity of initial P waveforms with nearby events. Among the new catalog events, we detect 513 repeating earthquakes (249 sequences, Table S2), including 235 doublets (470 events) and 14 multiplets (43 events). This indicates that only $\sim$1% of the earthquakes are repeaters, a

fraction significantly lower than that found in other regions, e.g. $\sim$10% in the NE Japan subduction zone (Igarashi et al., 2003). This can be explained by the much lower slip rate ($\sim$1 mm/yr) in our study region than the $\sim$8 cm/yr rate in the NE Japan subduction zone. We only find doublet-type repeaters in the time period between the M 6.4 and the M 7.1 events. Their recurrence times range from seconds to hours, indicating burst-type repeaters (e.g., Igarashi et al., 2003, Templeton et al., 2008). They are distributed along both the NW-striking and SW-striking fault zones (Fig. 2a). There are no repeaters at the location of large coseismic slip during the M 6.4 event, although seismicity is active. In comparison, doublet-type repeaters after the M 7.1 event are distributed across a broader region, although a lack of repeaters is observed in a region to the south of the M 7.1 epicenter (Fig. 3a). Some of the doublet-type repeaters might reflect the vigorous aftershock period when two events may have a chance of recurring at effectively the same location. The multiplet-type repeaters with at least 3 events in a sequence occur at locations devoid of large coseismic slip during the M 7.1 event (Fig. 3a). The recurrence times for individual multiplet-type repeaters show complexities (Figs. 3b-3d), with most of them exhibiting an increase in the recurrence time with time after M 7.1, consistent with the Omori's law (Figure S5). The repeater occurrences at locations surrounding principal coseismic slip patches appear to be consistent with a scenario where repeated ruptures are triggered by stress-driven afterslip in
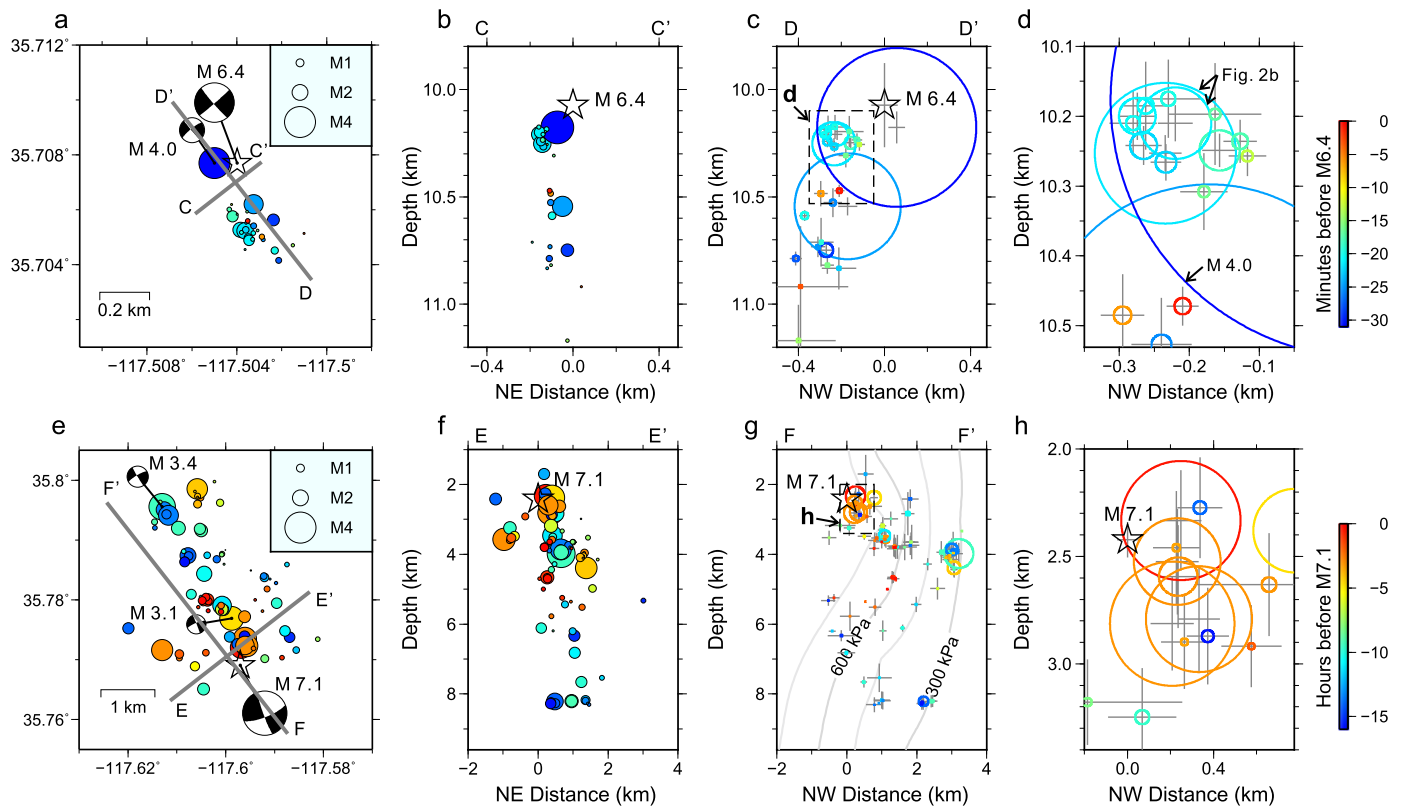
Fig. 4. Foreshock sequences of the M 6.4 and M 7.1 events. (a) Map view of the sequence, with events (circles) sized by magnitude and color coded by the time (in minutes) before the M 6.4 event, whose hypocenter is shown by the star. (b) The cross section of the seismicity in the cross-strike direction. (c) shows the fault-plane view of the sequence events sized by the source radius, which is estimated assuming a stress drop estimated from source analysis (see text for details) or 3 MPa if the stress drop is not constrained. (d) shows zoom-in of the dashed box in (c). The waveforms for the repeater doublet in (d) are shown in Fig. 2b. (e)-(g) are similar to (a)-(c) but for the foreshock sequence within 16 hours before the M 7.1 event. The gray curves in (g) denote the contours of Coulomb stress change imparted by the M 6.4 coseismic slip (Figure S11, Wang et al., 2020). (h) shows zoom-in of the dashed box in (g).

velocity-strengthening zones (e.g., Huang et al., 2017). Due to the very low fault slip rates in the study region, repeating earthquake sequences would be expected to recur at extremely long time intervals. Therefore, the search for repeaters within a longer time period and combined analysis with geodetic observations (e.g., Wang et al., 2020) can potentially further validate the possible afterslip transients, which is beyond the scope of this paper.

In the following, we show the seismicity evolution documented by our refined event catalog illuminates the nucleation processes of the M 6.4 and M 7.1 events. We observe an immediate foreshock sequence preceding the M 6.4 event, consistent with the recent study by Ross et al. (2019). This foreshock sequence started from the largest M 4.0 event (∼ 31 minutes before), followed by smaller events that are located deeper and to the southeast (Figs. 4a and 4b). Before the M 4.0 event, there were intermittent episodes of seismicity around the M 6.4 and M 7.1 epicenters (Figure S6). Those events around the M 6.4 epicenter occurred at depths of ∼ 10.9 km and within the M 4.0 rupture zone, indicating that they are foreshocks during 1-2 hours before the M 4.0 event (Figures S6a and S6b). In contrast, the events around the M 7.1 epicenter are deep (9-11 km depth) and occurred > 3 km away from the M 7.1 epicenter. These events likely reflect deformation episodes off the fault zone that are not directly related to the nucleation process (Figures S6c and S6d). The small gap (∼ 0.2 km) between epicenters of the M 4.0 event and other smaller events (Fig. 4a) might reflect the extent of the main coseismic slip area of the M 4.0 event. The foreshock sequence is aligned in the NW-SE direction, suggesting that the NW-striking nodal plane of the M 4.0 focal solution represents the fault plane. To inspect whether the source areas of the foreshock sequence overlap, we project the

seismicity onto the fault plane. The source sizes depend on the stress drops. We calculate the stress drop following the spectral decomposition method (Shearer et al., 2006, Trugman and Shearer, 2017b) for the M 1 - 4 events within a 5 km by 5 km box centered around the M 6.4 event (Text S1 and Figure S7). The estimated stress drop of the M 4.0 event is ∼ 50 MPa (Table S3). If the stress drop is not constrained, we simply assume it to be 3 MPa. Each event is generally located within one to two source dimensions of another earlier event (Fig. 4c). One repeater doublet is identified among this sequence, with a very short recurrence time of 23 sec (Figs. 4d and 2b). The M 6.4 hypocenter is at ∼ 0.45 km from the last event but close to the M 4.0 foreshock. Considering the source location uncertainties, it is not clear whether the M 6.4 hypocenter is located inside, or alternatively near the edge of the M 4.0 rupture area.

To investigate the seismicity evolution between the M 6.4 event and M 7.1 mainshock, we divide the NW-striking fault zone into seven sub-regions (Fig. 5). We also divide the time period according to an M 5.4 event that occurred ∼ 16 hours before the M 7.1 mainshock (Figs. 5a and 5b). The relative horizontal and depth errors based on bootstrapping 100 times the differential travel-time data (Trugman and Shearer, 2017a) are about 123 m and 215 m (Table S1), respectively. The apparent wide (∼2 km) surface projection of the seismicity zone is due to the complex fault geometry involving both NW and NE trending structures and the dipping angles changing with depth (Fig. 5). It is notable that the M 7.1 event nucleated at a depth of ∼ 2.4 km, much shallower than the M 6.4 event (∼ 10.1 km). The seismicity appears to migrate to shallower depths and also to the northwest leading up to the M 7.1 mainshock (Figs. 1b and 5). This pattern is also consistently seen
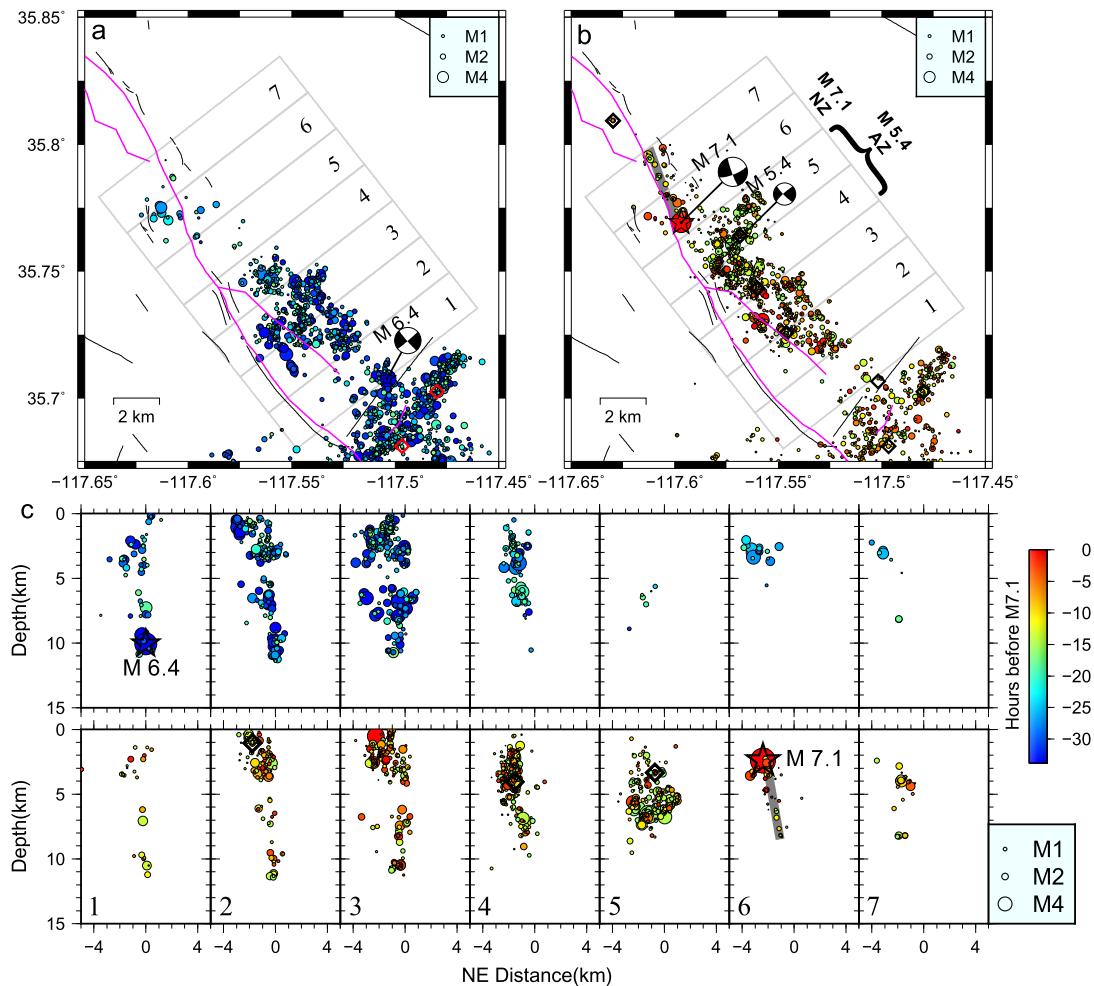
Fig. 5. The seismicity evolution from the M 6.4 event to the M 5.4 event (a) and from the M 5.4 event to the M 7.1 mainshock (b). (c) Comparison of cross sections of seismicity from the M 6.4 to the M 5.4 event (upper row) and from the M 5.4 event to the M 7.1 mainshock (bottom row). The seismicity is projected onto the SW-NE direction (long side of Region 1) with the origin at the M 6.4 epicenter. The events are sized by magnitude and colored by the hours before the M 7.1 mainshock. The focal mechanisms of the three events were obtained from USGS. The thick gray lines in (b) and (c) roughly depict the fault plane based on seismicity. M 5.4 AZ: M 5.4 aftershock zone; M 7.1 NZ: M 7.1 nucleation zone. Black diamonds denote the identified repeating earthquake doublets.

in other studies (Ross et al., 2019, Lin, 2020, Lomax, 2020, Shelly, 2020), although the absolute locations differ slightly between the catalogs (Figures S8-S10). We consider our catalog provides a more accurate estimation of the M 6.4 and M 7.1 hypocenters relative to other events due to the precise differential P travel times measured from short-window cross-correlation of only the initial onset phase. The absolute locations of events depend on the accuracy of arrival-time picking, station coverage and velocity model. Further improvements can be potentially made through joint inversion of the velocity model and events location (e.g., Zhang and Thurber, 2003) using more accurate absolute arrival-times enabled by deep-learning phase picking algorithms (Ross et al., 2018).

In Region 1 - 3, the seismicity rate increases abruptly after the M 6.4 event and decays with time. This seismicity can be considered the aftershocks of the M 6.4 coseismic rupture. The M 5.4 event clearly activates the intense seismicity within Region 5, which appears to extend onto a SW-striking fault plane perpendicular to the mainshock rupture (Fig. 5b). Therefore it is likely that the SW striking left-lateral nodal plane ruptured during the M 5.4 event (Shelly, 2020). The seismicity rates within Region 4 - 5 exhibit a significant increase immediately after the M 5.4 event, and then decay with time (Fig. 6). As such, we interpret regions 4 and 5 as the aftershock zone of the M 5.4 event (Fig. 5b). After the M 5.4 event, seismicity in a wider depth range (2-8 km) was activated within Region 6 (Fig. 5c). The events during the final hours

preceding the mainshock delineate a plane with a strike ($\sim$ 160°) and dip ($\sim$ 80°) consistent with the SE-striking nodal plane (160°, 84°) of the M 7.1 event (see thick gray lines in Figs. 5b and 5c). At $\sim$ 3 hours before the M 7.1 event, the seismicity rate in Region 6 rises again and stays elevated until the occurrence of the mainshock (Fig. 6f). The cross section of seismicity within Region 6 - 7 (from M 5.4 to M 7.1) shows that the mainshock hypocenter is located at the upper edge of the foreshock zone (Figs. 4e-4f). The projection onto the fault plane shows that some source rupture zones appear to overlap, but no repeaters are found in the sequence (Figs. 4g-4h). Considering location uncertainties, these events may reflect ruptures on closely spaced fault patches. The M 7.1 hypocenter is located at the edge of the rupture zone of the last event in the sequence (Fig. 4h). The finite fault solution of the M 6.4 earthquake (Wang et al., 2020) indicates that Region 6 and 7 experienced consistent positive Coulomb stress changes ranging from 250 to 770 kPa in the depth range of 0 - 10 km (Figs. 4g and S11). Therefore, the widely distributed foreshocks are likely caused by the static triggering effect of the M 6.4 rupture.

We estimate the b values by excluding the initial aftershocks which may be highly incomplete and heterogeneous (Gulia and Wiemer, 2019). The overall Mc is $\sim$ 0.9 and b value is $\sim$ 0.73 for all the seismicity within Region 1 - 7 between the M 6.4 and M 7.1 events (Figure S12). We also estimate the b value within individual regions. It appears that the b value in Region 6 ($\sim$ 0.48), where the
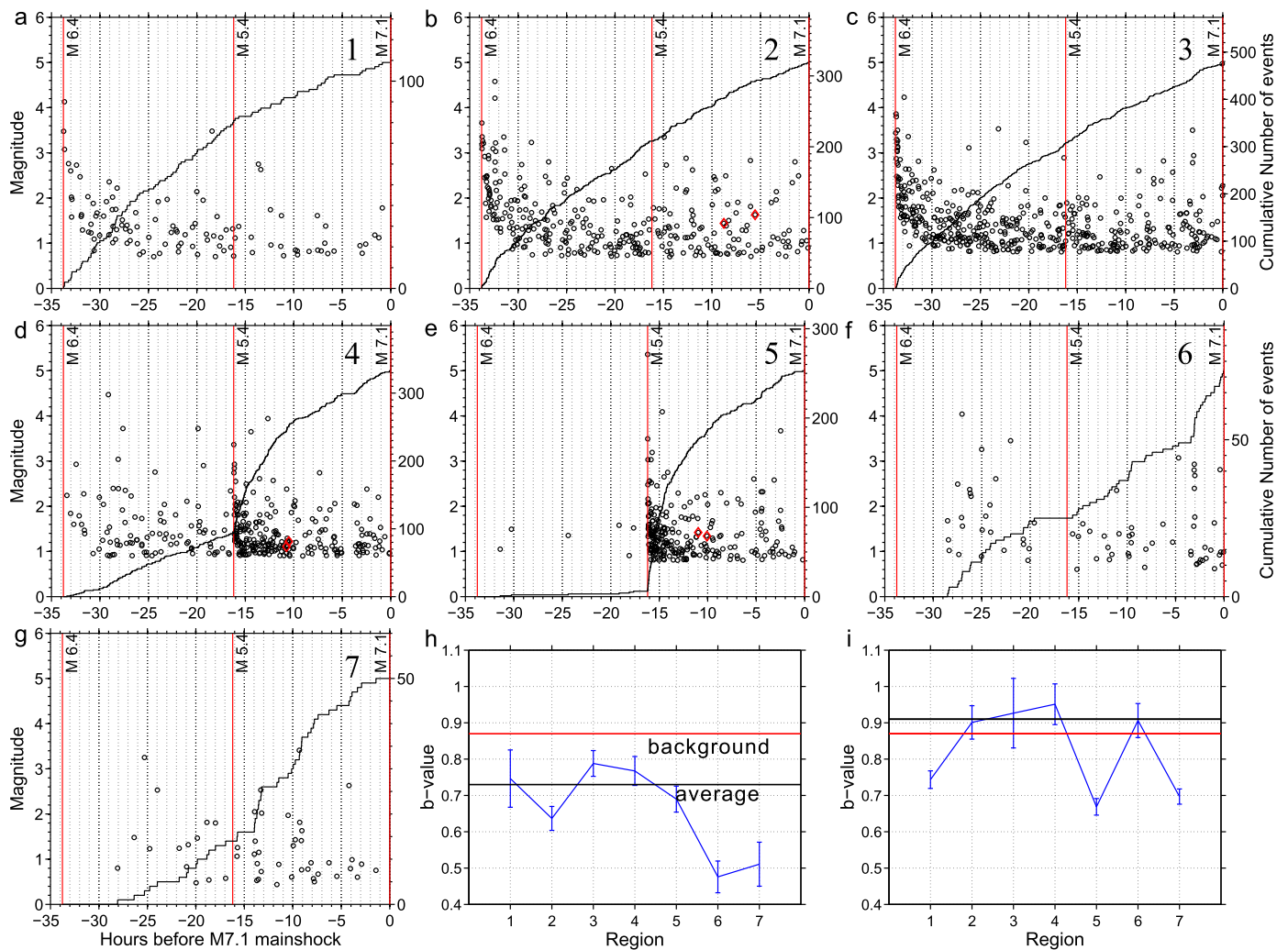
Fig. 6. (a)-(g) Cumulative number of events within regions 1-7 (Fig. 5) between the M 6.4 and M 7.1 earthquakes. The magnitude of completeness and b values are estimated individually in each region. Red symbols mark repeating earthquake pairs with the same symbol representing the same group. (h) shows the b values within regions 1-7 for seismicity between the M 6.4 and M 7.1 events (Figs. 5 and S13), revealing especially low b values within regions 6 and 7. The error bars show the standard deviations. The black horizontal line denotes the average b value estimated from all seismicity within regions 1-7 (from M 6.4 to M 7.1), while the red line denotes the pre-M6.4 background b value (Figure S14). (i) is similar to (h) but for seismicity from the M 7.1 event to 1 August 2019.

M 7.1 event nucleated, is particularly low compared to the other regions (Fig. 6h). It should be noted that although the number of events in Region 6 is less than 100, the frequency-magnitude distribution is reasonably well fit in the magnitude range of 0.5 - 3 (Figure S13). The b values between the M 6.4 and M 7.1 events appear to be significantly lower than the background b value (0.87 ± 0.03) in the area, which is estimated from the seismicity in a long time period (from 1 January 2000 to 4 July 2019, SCEDC catalog) before the M 6.4 event (Figure S14). This estimate is consistent with the b value within Region 1-7 (0.93 ± 0.14) inferred from our catalog from 1 January 2019 to the M 6.4 event (Figure S12a). During the period from the M 7.1 event to 1 August 2019, the overall b value (0.91 ± 0.01) and the individual b values in Region 1 - 7 (0.67 - 0.95) rise to near or above the background b value (Figs. 6i and S12d).

One concern of estimating b values from a matched-filter enhanced catalog is that the magnitudes of the small detected events may have relatively large uncertainties. We inspect the b-value variations for two other catalogs also built from matched-filter detection (Ross et al., 2019, Shelly, 2020). We also test the effect of magnitude of completeness (Mc) by adding different Mc correction values (0 - 0.4): the minimum magnitude Mmin = Mc + 0, 0.2 and 0.4. The absolute b values differ between different cata-

logs but the relatively low b value in Region 6-7 after M 6.4 and before M 7.1 and overall increase of b value after M 7.1 are consistently observed (Fig. 7). It is also worth noting that the relatively low b value for seismicity around the M 7.1 epicenter (Region 6-7) from M 6.4 to M 7.1 is calculated based on a small dataset (∼ 150 events). To more fairly assess its significance, we estimate b values from an equal number of 150 random events in different space-time windows. We repeat this procedure 1000 times to generate the b value distribution for each window. The result shows that the b value distributions in the background period (a 20-km radius circular area), from M 6.4 to M 7.1 (Region 1-5 and profile BB') and after M 7.1 (Region 1-7 and profile BB') largely overlap (Figs. 8a-8b). However, the b value distribution around the M 7.1 hypocenter (Region 6-7, from M 6.4 to M 7.1) is significantly lower and well separated from those of the other space-time windows (Fig. 8b).

4. Discussion and conclusion

In this study, we apply the matched-filter detection to obtain a complete (Mc = 0.9) and accurate earthquake catalog during the 2019 M 6.4 and M 7.1 Ridgecrest earthquake sequence. Our results reveal aligned foreshock sequences concentrated near the hypocen-
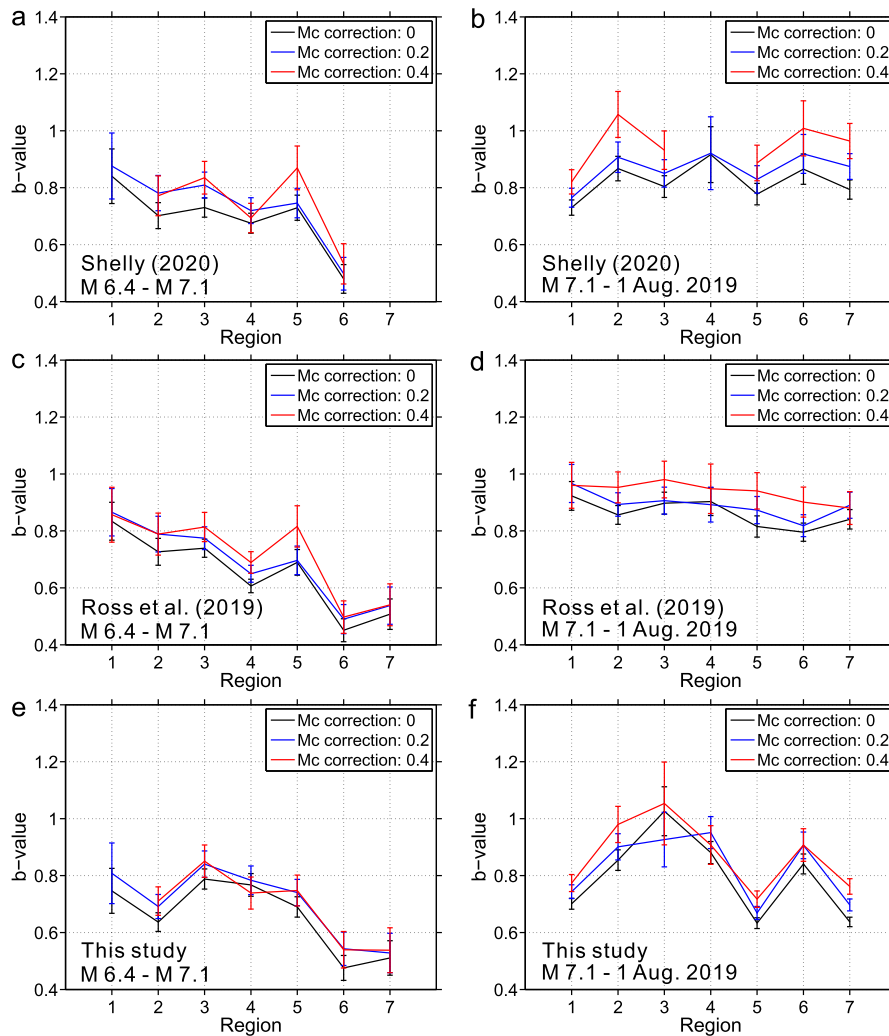
Fig. 7. Comparison of the b value estimation for different catalogs (Shelly, 2020, Ross et al., 2019) within Region 1-7 (Fig. 5). Three different corrections of Mc (0 - 0.4), which mean that minimum magnitude Mmin = Mc + 0, 0.2 and 0.4, are used to test the effect of Mc on the observed b-value variations. Some cases fail to give an estimate of b value due to the lack of minimum number of events (30) above the magnitude completeness.

ters of both the M 6.4 and M 7.1 events, which are inferred to be related to the nucleation process of the respective mainshocks. We discuss the spatio-temporal evolution of the foreshock sequences and their implications for the nucleation processes of the M 6.4 and M 7.1 events.

4.1. Foreshock sequences and insights into nucleation processes

It is still controversial whether cascade triggering or pre-slip mechanisms are the dominant physical mechanisms during foreshock sequences. Preslip could be either a phase of slow slip which accelerates into dynamic rupture (e.g., Tape et al., 2018), or simply be a slow slip episode that happens to trigger a larger earthquake (e.g., Radiguet et al., 2016). Laboratory studies and numerical simulations generally find a phase of slip acceleration preceding the mainshock (e.g., Ampuero and Rubin, 2008, Dublanchet, 2018, McLaskey, 2019). Recent studies show that the foreshock sequences of the 1999 M 7.6 Izmit and the 1999 M 7.1 Hector Mine earthquakes are consistent with the cascade triggering process (Ellsworth and Bulut, 2018, Yoon et al., 2019) whereas the foreshocks of the 1992 M 7.4 Landers earthquake appear to support the slow slip model (Dodge et al., 1996). For the case of the 2019 Ridgecrest earthquake sequence, the M 6.4 event was preceded by a 31-minute-long foreshock sequence which started with the largest M 4.0 event. The M 4.0 event was followed by

smaller events, suggesting a triggered aftershock sequence. As each event is generally located within one to two source dimensions of another earlier event, the overall evolution of the sequence is consistent with the cascade triggering model. The M 6.4 hypocenter is possibly located inside, or alternatively near the edge of the rupture zone of the largest M 4.0 foreshock. For the first case, aseismic slip might be required to reload the M 6.4 nucleation area that already ruptured in the M 4.0 event. For the latter case, the M 6.4 hypocenter is likely to be loaded by the static stress transfer by the M 4.0 event and the subsequent smaller events. The rapidly recurring repeating-earthquake doublet found in this sequence (Figs. 2b and 4d) might suggest small-scale local aseismic transients. If appropriate observations are available, future work may involve solving for the M 4.0 coseismic slip distribution to investigate whether the M 6.4 event re-ruptured part of the M 4.0 rupture zone.

Our observations also provide insights into the initiation of the M 6.4 rupture. The NW-SE alignment of the foreshock sequence as shown in our observations is consistent with the initial NW-trending rupture segment suggested by the subevent analysis (Ross et al., 2019) and kinematic rupture models (Liu et al., 2019, Chen et al., 2020, Wang et al., 2020). The subevent analysis from regional waveforms found that the first subevent ruptured the NW trending segment, followed by subevents 2 and 3 along the SW segment
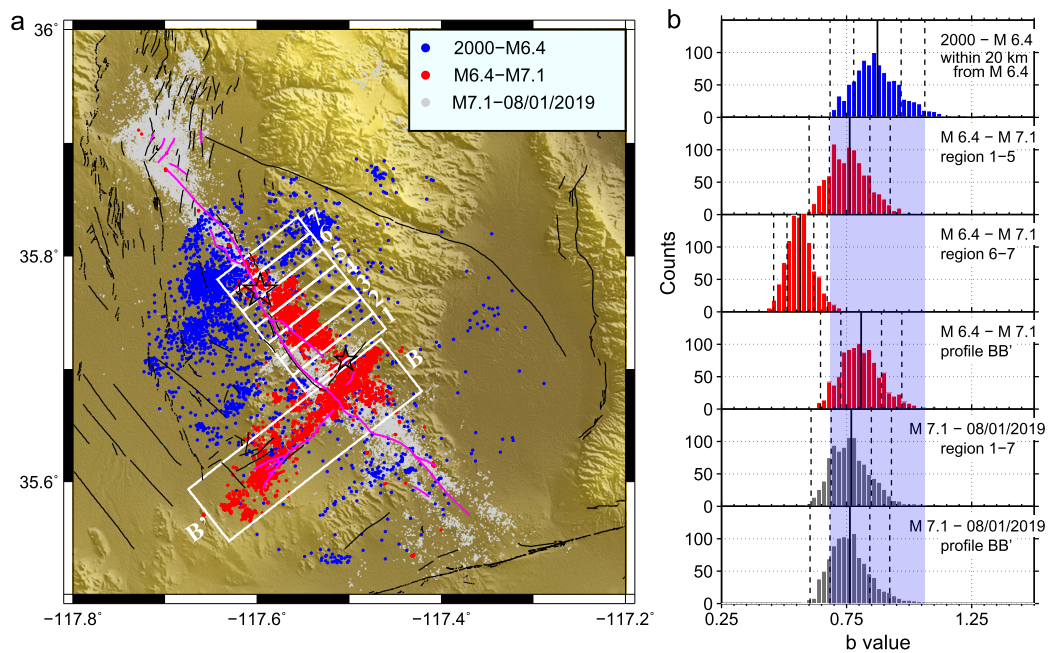
Fig. 8. Comparison of b-value distribution. (a) shows the seismicity with different colors denoting different time periods. Profiles BB' and Region 1-7 are the same as those in Figs. 1a and 5a. (b) shows the distribution of b value, estimated from a small number of events (150), in different space-time windows shown in (a). The b value is estimated based on 1000 randomly drawn subsets of 150 events. The vertical solid black lines denote the mean b value while the dashed lines mark the one and two standard deviations. The transparent areas denote the b value range within two standard deviations for the background period (blue, from 1 January 2000 to M 6.4).

(Ross et al., 2019). The kinematic rupture models showed that the M 6.4 event nucleated along a NW-striking fault, although the majority moment release was along the SW fault segment southwest of its epicenter (Liu et al., 2019, Chen et al., 2020, Wang et al., 2020).

The M 6.4 event was followed by a 34-hour-long earthquake sequence that led up to the M 7.1 event. Modeling of the cumulative static stress change showed that the M 6.4 event and the evolving earthquake sequence promoted the occurrence of the M 7.1 rupture (Barnhart et al., 2019). In particular, the M 6.4 and M 5.4 events imparted the largest Coulomb stress changes near the M 7.1 hypocenter. Our results provide additional information regarding the evolving sequence. Our observations illuminate the distinct evolution of seismicity in different regions along the NW trending fault zone. The M 5.4 event clearly expands the seismicity towards the M 7.1 epicenter and triggers an intense local aftershock sequence (see Regions 5-6 in Fig. 5). The final, 3-hour-long seismicity acceleration around the M 7.1 hypocenter, however, occurred ∼ 13 hours after the M 5.4 event. The physical mechanism of this delayed acceleration is not clear. It is possible that the M 5.4 event triggered aseismic transients (e.g., slow slip and/or fluid flow diffusion) that slowly redistributed the stress in surrounding regions. Yue et al. (2019) inverted strainmeter data for the slip distribution between the M 6.4 and M 7.1 earthquakes and resolved both coseismic slip of the M 5.4 event on the NW trending plane and decaying aseismic slip along both the NW and NE planes. The repeating earthquakes might support this hypothesis but only doublet-type repeaters were observed following the M 5.4 event (Figs. 5, 6b, 6d-6e). This may be limited by the temporal resolution of the repeater analysis in such a short time period.

The relation between the nucleation process and the mainshock magnitude is still under debate (e.g., Ellsworth and Beroza, 1995, Dodge et al., 1996, Chen and Shearer, 2016, Acosta et al., 2019, Yoon et al., 2019). For example, Dodge et al. (1996) observed a scaling relation between the radius of the foreshock zone and the mainshock moment for six strike-slip earthquakes in California (Fig. 9). Acosta et al. (2019) found that the mainshock moment scaled with the precursory moment (seismic + aseismic) in labora-
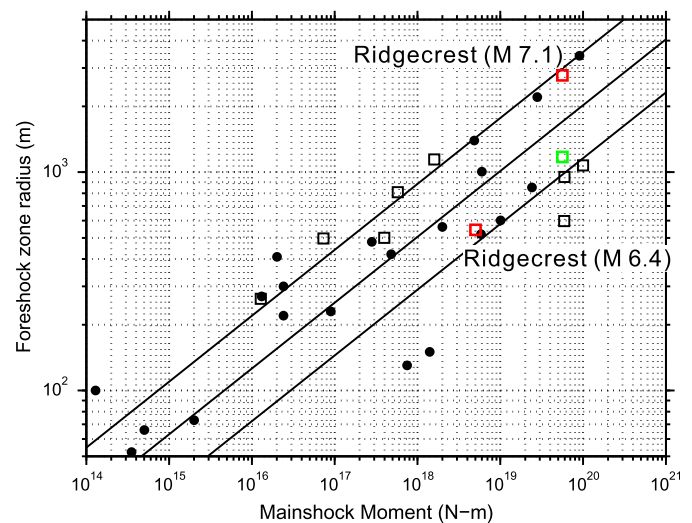

Fig. 9. The scaling relationship between the foreshock-zone radius and the mainshock moment, after Ellsworth and Beroza (1995), Dodge et al. (1996) and Yoon et al. (2019). The black dots and squares show the estimates from Ellsworth and Beroza (1995) and Dodge et al. (1996), respectively. The black lines denote the least-square fit and 1σ errors from Dodge et al. (1996). The two red squares denote our estimation of the foreshock-zone radius of the M 6.4 and M 7.1 events based on the foreshock sequences shown in Figs. 4c and 4g and determined following the procedure in Yoon et al. (2019). The green square shows the estimation of the M 7.1 foreshock-zone radius from the foreshocks within the last 3 hours which exhibit an acceleration phase (Fig. 6f).

tory experiments. In contrast, Chen and Shearer (2016) and Yoon et al. (2019) found no correlation between the size of the foreshock zone and the mainshock magnitude. We estimate the radius of the foreshock zone for the 2019 M 6.4 and M 7.1 Ridgecrest earthquakes based on the immediate foreshock sequence around the hypocenter (Figs. 4c and 4g). For the M 6.4 event, the foreshock-zone radius is estimated from the foreshock sequence starting with the largest M 4.0 foreshock. For the M 7.1 event, however, it is not straightforward to define the immediate foreshocks, since the pre-

ceding seismicity is also part of the M 6.4 aftershock sequence. As discussed above (Section 3), we consider the seismicity in Region 6 and 7 within the last 16 hours (from M 5.4 to M 7.1) or the last 3 hours (the acceleration phase, Fig. 6f) as the immediate foreshock sequence of the M 7.1 event. It appears that the observations of the M 6.4 and M 7.1 events agree with the scaling established by Dodge et al. (1996). Although the data points are scattered and further investigation of other foreshock sequences is warranted, our observations might be consistent with a preslip model that invokes a dependence of the mainshock magnitude on the nucleation process (e.g., McLaskey, 2019).

4.2. b-Value variations and implications on the stress conditions

Low b values around the eventual hypocentral area of large earthquakes have been observed in both laboratory experiments and various tectonic settings. Laboratory experiments showed a systematic decrease of b value preceding the entire fracture (e.g., Lei, 2003). Nanjo et al. (2012) observed a decade-long decrease of b value preceding the 2011 Mw 9.0 Tohoku (NE Japan subduction zone) and 2004 Mw 9.1 Sumatra (Sumatra subduction zone) earthquakes. Schurr et al. (2014) observed that the M 8.1 Iquique earthquake nucleated in an area of low b value, which gradually decreased starting three years before the mainshock. The b value has been suggested as a stress sensor with lower values indicating higher differential stresses (e.g., Scholz, 2015). Recent efforts attempted to adapt the short-term b-value variations into real-time earthquake hazard assessment. Gulia and Wiemer (2019) suggest that a significant drop of the b value in the aftershock volume of a moderate to large earthquake indicates that another large event may still occur, as low b values may suggest the presence of critically pre-stressed faults and/or high stress levels following the initial event. However, it is necessary to test this hypothesis with more examples as they put forward only two case examples, the 2016 Amatrice–Norcia and Kumamoto earthquake sequences, in their study (Brodsky, 2019).

Our results provide another example of low b values preceding a large earthquake within a major plate boundary zone that involves complex ruptures in multiple fault systems. The statistical analysis shows that the M 7.1 event nucleated in a region with a significantly reduced b value compared to the background time period (Fig. 8). This is consistent with the b-value observations in other recent studies (Gulia et al., 2020, Nanjo, 2020, Dascher-Cousineau et al., 2020). Therefore the Ridgecrest earthquake sequence appears to be another case to support the hypothesis by Gulia and Wiemer (2019). The significantly low b value may indicate that the M 7.1 nucleated in a region of high differential stress that was further enhanced by the M 6.4 and subsequent activity (Figs. 4g and S11, Barnhart et al., 2019). One issue of real-time mapping of b values is the limited size of cataloged events, especially around locked zones where large earthquakes may nucleate but the seismicity rate is usually low. Other issues include the strong dependence of b-value estimations on the choice of parameters, challenging its use for issuing short-term warnings (Dascher-Cousineau et al., 2020). Future developments may involve the near real-time detection of small events and determination of their magnitudes, potentially facilitated by machine learning algorithms (e.g., Ross et al., 2018). In addition, systematic and long-term statistical analysis is essential to further test the importance of b values in real-time hazard assessment and forecasting in southern California.

CRediT authorship contribution statement

Hui Huang: Conceptualization, Formal analysis, Methodology, Software, Writing - original draft, Writing - review & editing.

Lingsen Meng: Conceptualization, Funding acquisition, Writing - review & editing. **Roland Bürgmann:** Conceptualization, Supervision, Writing - review & editing. **Wei Wang:** Formal analysis, Software, Writing - review & editing. **Kang Wang:** Formal analysis, Writing - review & editing.

Declaration of competing interest

The authors declare that they have no known competing financial interests or personal relationships that could have appeared to influence the work reported in this paper.

Acknowledgements

Appendix A. Supplementary material

Supplementary material related to this article can be found online at https://doi.org/10.1016/j.epsl.2020.116582.

References

Acosta, M., Passelègue, F.X., Schubnel, A., Madariaga, R., Violay, M., 2019. Can precursory moment release scale with earthquake magnitude? A view from the laboratory. Geophys. Res. Lett. 46 (22), 12927–12937.

Ampuero, J.-P., Rubin, A.M., 2008. Earthquake nucleation on rate and state faults—aging and slip laws. J. Geophys. Res. 113, B01302.

Barnhart, W.D., Hayes, G.P., Gold, R.D., 2019. The July 2019 Ridgecrest, California earthquake sequence: kinematics of slip and stressing in cross-fault ruptures. Geophys. Res. Lett.

Bouchon, M., Karabulut, H., Aktar, M., Özalaybey, S., Schmittbuhl, J., Bouin, M.P., 2011. Extended nucleation of the 1999 Mw 7.6 Izmit earthquake. Science 331 (6019), 877–880.

Bouchon, M., Durand, V., Marsan, D., Karabulut, H., Schmittbuhl, J., 2013. The long precursory phase of most large interplate earthquakes. Nat. Geosci. 6 (4), 299–302.

Brodsky, E.E., 2019. Determining whether the worst earthquake has passed. Nature 574, 185–186.

Chen, K., Avouac, J.P., Aati, S., Milliner, C., Zheng, F., Shi, C., 2020. Cascading and pulse-like ruptures during the 2019 Ridgecrest earthquakes in the Eastern California Shear Zone. Nat. Commun. 11 (1), 1–8.

Chen, X., Shearer, P.M., 2016. Analysis of foreshock sequences in California and implications for earthquake triggering. Pure Appl. Geophys. 173 (1), 133–152.

Dascher-Cousineau, K., Lay, T., Brodsky, E.E., 2020. Two foreshock sequences Post Gulia and Wiemer (2019). Seismol. Res. Lett.

Dodge, D.A., Beroza, G.C., Ellsworth, W.L., 1996. Detailed observations of California foreshock sequences: implications for the earthquake initiation process. J. Geophys. Res. 101 (B10), 22,371–22,392.

Dublanchet, P., 2018. The dynamics of earthquake precursors controlled by effective friction. Geophys. J. Int. 212 (2), 853–871.

Ellsworth, W.L., Beroza, G.C., 1995. Seismic evidence for an earthquake nucleation phase. Science 268, 851–855.

Ellsworth, W.L., Bulut, F., 2018. Nucleation of the 1999 Izmit earthquake by a triggered cascade of foreshocks. Nat. Geosci. 11 (7), 531.

Gibbons, S.J., Ringdal, F., 2006. The detection of low magnitude seismic events using array-based waveform correlation. Geophys. J. Int. 165 (1), 149–166.

Gulia, L., Wiemer, S., 2019. Real-time discrimination of earthquake foreshocks and aftershocks. Nature 574 (7777), 193–199.

Gulia, L., Wiemer, S., Vannucci, G., 2020. Pseudoprospective evaluation of the foreshock traffic-light system in Ridgecrest and implications for aftershock hazard assessment. Seismol. Res. Lett.

Hill, D.P., Prejean, S.G., 2015. Dynamic triggering. In: Kanamori, H. (Ed.), Treatise on Geophysics, vol. 4, chap. 8, 2nd ed. Elsevier, Oxford, UK, pp. 273–304.

Huang, H., Xu, W., Meng, L., Bürgmann, R., Baez, J.C., 2017. Early aftershocks and afterslip surrounding the 2015 Mw 8.4 Illapel rupture. Earth Planet. Sci. Lett. 457, 282–291.

Huang, H., Meng, L., 2018. Slow unlocking processes preceding the 2015 Mw 8.4 Illapel, Chile, earthquake. Geophys. Res. Lett. 45 (9), 3914–3922.

Hutton, K., Woessner, J., Hauksson, E., 2010. Earthquake monitoring in southern California for seventy-seven years (1932–2008). Bull. Seismol. Soc. Am. 100 (2), 423–446.

Igarashi, T., Matsuzawa, T., Hasegawa, A., 2003. Repeating earthquakes and interplate aseismic slip in the northeastern Japan subduction zone. J. Geophys. Res., Solid Earth 108 (B5).

Kato, A., Obara, K., Igarashi, T., Tsuruoka, H., Nakagawa, S., Hirata, N., 2012. Propagation of slow slip leading up to the 2011 Mw 9.0 Tohoku-Oki earthquake. Science 335 (6069), 705–708.

Lei, X., 2003. How do asperities fracture? An experimental study of unbroken asperities. Earth Planet. Sci. Lett. 213 (3–4), 347–359.

Lengliné, O., Marsan, D., 2009. Inferring the coseismic and postseismic stress changes caused by the 2004 Mw = 6 Parkfield earthquake from variations of recurrence times of microearthquakes. J. Geophys. Res. 114, B10303.

Lin, G., 2020. Waveform cross-correlation relocation and focal mechanisms for the 2019 Ridgecrest earthquake sequence. Seismol. Res. Lett.

Liu, C., Lay, T., Brodsky, E.E., Dascher-Cousineau, K., Xiong, X., 2019. Coseismic rupture process of the large 2019 Ridgecrest earthquakes from joint inversion of geodetic and seismological observations. Geophys. Res. Lett. 46 (21), 11820–11829.

Lomax, A., 2020. Absolute location of 2019 Ridgecrest seismicity reveals a shallow Mw 7.1 hypocenter, migrating and pulsing Mw 7.1 foreshocks, and duplex Mw 6.4 ruptures. Bull. Seismol. Soc. Am.

McLaskey, G.C., 2019. Earthquake initiation from laboratory observations and implications for foreshocks. J. Geophys. Res., Solid Earth 124.

Meng, L., Huang, H., Bürgmann, R., Ampuero, J.P., Strader, A., 2015. Dual megathrust slip behaviors of the 2014 Iquique earthquake sequence. Earth Planet. Sci. Lett. 411, 177–187.

Milliner, C., Donnellan, A., 2020. Using daily observations from planet labs satellite imagery to separate the surface deformation between the 4 July Mw 6.4 foreshock and 5 July Mw 7.1 mainshock during the 2019 Ridgecrest earthquake sequence. Seismol. Res. Lett.

Nanjo, K.Z., 2020. Were changes in stress state responsible for the 2019 Ridgecrest, California, earthquakes?. Nat. Commun. 11 (1), 3082.

Nanjo, K.Z., Hirata, N., Obara, K., Kasahara, K., 2012. Decade-scale decrease in b value prior to the M9-class 2011 Tohoku and 2004 Sumatra quakes. Geophys. Res. Lett. 39 (20).

Ogata, Y., Katsura, K., 2014. Comparing foreshock characteristics and foreshock forecasting in observed and simulated earthquake catalogs. J. Geophys. Res., Solid Earth 119, 8457–8477.

Peng, Z., Zhao, P., 2009. Migration of early aftershocks following the 2004 Parkfield earthquake. Nat. Geosci. 2 (12), 877.

Petruccelli, A., Schorlemmer, D., Tormann, T., Rinaldi, A.P., Wiemer, S., Gasperini, P., Vannucci, G., 2019. The influence of faulting style on the size-distribution of global earthquakes. Earth Planet. Sci. Lett. 527, 115791.

Radiguet, M., Perfettini, H., Cotte, N., Gualandi, A., Valette, B., Kostoglodov, V., Campillo, M., 2016. Triggering of the 2014 Mw 7.3 Papanoa earthquake by a slow slip event in Guerrero, Mexico. Nat. Geosci. 9 (11), 829.

Ross, Z.E., Meier, M.A., Hauksson, E., 2018. P wave arrival picking and first-motion polarity determination with deep learning. J. Geophys. Res., Solid Earth 123 (6), 5120–5129.

Ross, Z.E., Idini, B., Jia, Z., Stephenson, O.L., Zhong, M., Wang, X., Hauksson, E., 2019. Hierarchical interlocked orthogonal faulting in the 2019 Ridgecrest earthquake sequence. Science 366 (6463), 346–351.

Scholz, C.H., 2015. On the stress dependence of the earthquake b value. Geophys. Res. Lett. 42 (5), 1399–1402.

Schurr, B., Asch, G., Hainzl, S., Bedford, J., Hoechner, A., Palo, M., et al., Oncken, O., 2014. Gradual unlocking of plate boundary controlled initiation of the 2014 Iquique earthquake. Nature 512 (7514), 299–302.

Seif, S., Zechar, J.D., Mignan, A., Nandan, S., Wiemer, S., 2018. Foreshocks and their potential deviation from general seismicity. Bull. Seismol. Soc. Am., 109.

Shearer, P.M., Prieto, G.A., Hauksson, E., 2006. Comprehensive analysis of earthquake source spectra in southern California. J. Geophys. Res., Solid Earth 111 (B6).

Shearer, P.M., 2012. Self-similar earthquake triggering, Båth's law, and foreshock/aftershock magnitudes: simulations, theory, and results for southern California. J. Geophys. Res., Solid Earth 117 (B6).

Shelly, D.R., Beroza, G.C., Ide, S., 2007. Non-volcanic tremor and low-frequency earthquake swarms. Nature 446 (7133), 305.

Shelly, D.R., Ellsworth, W.L., Hill, D.P., 2016. Fluid-faulting evolution in high definition: connecting fault structure and frequency-magnitude variations during the 2014 Long Valley Caldera, California, earthquake swarm. J. Geophys. Res., Solid Earth 121.

Shelly, D.R., 2020. A high-resolution seismic catalog for the initial 2019 Ridgecrest earthquake sequence: foreshocks, aftershocks, and faulting complexity. Seismol. Res. Lett.

Socquet, A., Valdes, J.P., Jara, J., Cotton, F., Walpersdorf, A., Cotte, N., Norabuena, E., 2017. An 8 month slow slip event triggers progressive nucleation of the 2014 Chile megathrust. Geophys. Res. Lett. 44 (9), 4046–4053.

SCEDC, 2013. Southern California Earthquake Data Center. Caltech. Dataset. https://doi.org/10.7909/C3WD3xH1.

Tape, C., Holtkamp, S., Silwal, V., Hawthorne, J., Kaneko, Y., Ampuero, J.P., West, M.E., 2018. Earthquake nucleation and fault slip complexity in the lower crust of central Alaska. Nat. Geosci. 11 (7), 536.

Templeton, D.C., Nadeau, R.M., Bürgmann, R., 2008. Behavior of repeating earthquake sequences in central California and the implications for subsurface fault creep. Bull. Seismol. Soc. Am. 98 (1), 52–65.

Trugman, D.T., Shearer, P.M., 2017a. GrowClust: a hierarchical clustering algorithm for relative earthquake relocation, with application to the Spanish Springs and Sheldon, Nevada, earthquake sequences. Seismol. Res. Lett. 88 (2A), 379–391.

Trugman, D.T., Shearer, P.M., 2017b. Application of an improved spectral decomposition method to examine earthquake source scaling in Southern California. J. Geophys. Res., Solid Earth 122 (4), 2890–2910.

Uchida, N., Bürgmann, R., 2019. Repeating earthquakes. Annu. Rev. Earth Planet. Sci. 47, 305–332.

Uchida, N., Matsuzawa, T., 2013. Pre- and postseismic slow slip surrounding the 2011 Tohoku-oki earthquake rupture. Earth Planet. Sci. Lett. 374, 81–91.

Waldhauser, F., Schaff, D.P., 2008. Large-scale relocation of two decades of northern California seismicity using cross-correlation and double-difference methods. J. Geophys. Res., Solid Earth 113 (B8).

Wang, K., Dreger, D., Tinti, E., Bürgmann, R., Taira, T., 2020. Rupture process of the 2019 Ridgecrest, California Mw 6.4 foreshock and Mw 7.1 earthquake constrained by seismic and geodetic data. Bull. Seismol. Soc. Am. https://doi.org/10.1785/0120200108.

Wiemer, S., 2001. A software package to analyze seismicity: ZMAP. Seismol. Res. Lett. 72 (3), 373–382.

Yoon, C.E., Yoshimitsu, N., Ellsworth, W.L., Beroza, G.C., 2019. Foreshocks and mainshock nucleation of the 1999 Mw 7.1 Hector Mine, California, earthquake. J. Geophys. Res., Solid Earth 124 (3), 1569–1582.

Yue, H., Sun, J., Wang, M., Shen, Z., Zhou, Y., Lu, W., Xue, L., 2019. Seismic and aseismic slips contributed to the foreshock-to-mainshock triggering during the July 2019 Ridgecrest earthquake sequence. In: AGU Fall Meeting 2019. AGU.

Zhang, H., Thurber, C.H., 2003. Double-difference tomography: the method and its application to the Hayward fault, California. Bull. Seismol. Soc. Am. 93 (5), 1875–1889.